

# Homodyne readout for a single KID

O. Castellano, M. D'Astolfo and R. Gargiulo

September 5, 2021

## Abstract

Kinetic Inductance Detectors, or KIDs, are cryogenic detectors that stood out since 2003 due to their high sensitivity, low thermal noise and natural multiplexing.

KIDs work on the principle that incident energy changes the surface impedance of a superconductor that is placed in a resonant circuit, so that the signal is seen as a change of the frequency and the shape of the resonance.

In this paper we report the design, the implementation and the operation of a homodyne readout and a Data Acquisition System for a single KID architecture. We were able to calibrate the detector, to estimate its resolution ( $(733 \pm 68)$  eV) and to measure the energy of the Fe-55 K-alpha X-ray peak (5.89 keV), obtaining  $(6.0 \pm 1.9)$  keV.

# Contents

<b>1</b>	<b>Introduction</b>	<b>3</b>
<b>2</b>	<b>Theoretical foundations</b>	<b>3</b>
2.1	Low-temperature detectors . . . . .	3
2.2	Electrodynamics of superconductors . . . . .	3
2.2.1	Kinetic Inductance . . . . .	4
<b>3</b>	<b>Working principle</b>	<b>5</b>
<b>4</b>	<b>Experimental setup</b>	<b>7</b>
4.1	Cryostat . . . . .	7
4.2	Readout concept . . . . .	8
4.3	Radio frequency circuit . . . . .	10
4.3.1	IQ mixer . . . . .	10
4.4	Baseband circuit . . . . .	12
4.4.1	Anti-aliasing filter . . . . .	13
4.4.2	Amplifier and Summing Circuit . . . . .	14
4.5	Data Acquisition . . . . .	14
4.5.1	Digitizer . . . . .	14
4.5.2	Online trigger . . . . .	15
4.5.3	DAQ procedure . . . . .	16
<b>5</b>	<b>Data Analysis</b>	<b>17</b>
5.1	IQ mixer calibration . . . . .	17
5.2	Signals reconstruction . . . . .	18
5.2.1	Signal sources . . . . .	18
5.2.2	Smoothing . . . . .	19
5.2.3	Events selection . . . . .	20
5.3	Calibration . . . . .	21
5.4	Fe-55 X-ray peak search . . . . .	22
<b>6</b>	<b>Methods</b>	<b>24</b>
<b>7</b>	<b>Conclusion</b>	<b>24</b>

# 1 Introduction

Kinetic Inductance Detectors are superconducting resonators suitable for a large variety of radiation and particle detectors. They have been first developed by scientists at the California Institute of Technology and the Jet Propulsion Laboratory in 2003 as phonon detectors [2]. They are used for a range of astronomy applications, including optical, infrared and millimeter wavelength phonon detection (for instance at the Caltech Submillimeter Observatory [5]).

Their main advantages are high sensitivity, low thermal noise and natural multiplexing. As a matter of fact, it is possible to read several KIDS, by appropriately placing the resonant frequencies, using only one transmission line.

Since their natural frequency multiplexing allows KIDs to achieve small detector package sizes, KIDs have also gained popularity as a more compact and less massive alternative to transition edge sensors. For these reasons an important effort is being made in order to adapt them to particle physics using an array of KIDS on a silicon substrate [6], especially in the fields of neutrino physics and dark matter direct detection [3] [7].

In this paper we report the design, the implementation and the operation of a readout apparatus and a Data Acquisition System for a single KID architecture. The detector we used was provided and installed by our tutors M. Vignati and A. Cruciani; a complete description of it can be found in [3].

In order to explain in detail the operational principle of KIDS it is useful to briefly review some theoretical aspects [2].

## 2 Theoretical foundations

### 2.1 Low-temperature detectors

Cryogenic detectors have been a subject of intense interest because of the desire to do experiments in particle and astroparticle physics that require very high energy resolution and sensitivity to small energy depositions. These detectors work at very low-temperatures, often well below 1 K, to minimize the noise in the measurements, and are usually used to sense small signals. The reason behind their high energy resolution is that they can exploit phenomena that require a little amount of energy deposit to generate a signal ( $E \sim meV$ ). The key elements that mark the building setup of a cryogenic detector are the:

- **Thermal bath**, which cools down the apparatus;
- **Absorber**, the sensitive part of the device where particles release their energy;
- **Sensor**, which allows to convert the thermal variation of the absorber in an electrical signal.

### 2.2 Electrodynamics of superconductors

A superconductor is a material that below its critical temperature  $T_c$  has zero resistance for DC currents but a non-zero impedance for AC currents. At very low-temperatures, electrons

do not scatter on the lattice anymore and are bound in Cooper pairs: couples of electrons with opposite spin, which behave as bosons. The binding energy for a single pair is constant and higher than the thermal energy (when  $T \ll T_c$ ) and is approximately given by:

$$E_B = 3.5k_B T_c \quad (1)$$

As a consequence of their bosonic behavior, Cooper pairs can condense and share the same wave function: therefore, they move in the superconductor in a completely ordered way, without any energy dissipation. In addition, a superconductor will expel almost all the magnetic field lines from its bulk and only allow the penetration of magnetic fields within a small distance (typically  $10 - 100 \text{ nm}$ ) from the surface, known as London penetration depth:

$$\lambda_L = \sqrt{\frac{m_e}{\mu_0 n_{cp} e^2}} \quad (2)$$

where  $m_e$  is the mass of an electron,  $e$  is its electric charge,  $\mu_0$  is the vacuum permeability and  $n_{cp}$  the density of Cooper pairs. In our case  $\lambda_L = 16 \text{ nm}$  and  $E_B = 3.5 \cdot 10^{-4} \text{ eV}$ , because we are using an aluminium superconductor with a  $T_c = 1.2 \text{ K}$ .

### 2.2.1 Kinetic Inductance

The surface impedance is the fundamental parameter that determines the characteristic behaviour of KIDs. We will briefly review it, in order to have a clear picture of its physical meaning.

The impedance of a superconducting strip can be split into an imaginary part, which is the total inductance, and a real part, which is the resistance. We will only focus on the imaginary part, as in a superconductor the dissipation is extremely small and all the energy is stored through kinetic inductance.

The total inductance of a superconducting strip includes two parts: a kinetic inductance ( $L_k$ ) and a magnetic inductance ( $L_m$ ),

$$L_{tot} = L_k + L_m \quad (3)$$

If we take into account the case where an electric field is applied near the surface of a superconductor, the kinetic inductance is associated with the kinetic energy of the superconducting electrons that are accelerated back and forth in the material by the electric field. On the other hand, the magnetic inductance is associated with the magnetic field generated by the current in the conductor. The behaviour of  $L_k$  is very different from the  $L_m$  one: its value depends not only on geometrical factors, but also on the density of bound electrons, and, thus, on the temperature. At the thickness of our superconductive strip (about  $60 \text{ nm}$ ) we have  $L_k = 3\% L_m$ .

In order to express  $L_k$  quantitatively, we could go to the limit  $t \ll \lambda_L$ , where  $t$  is the thickness of the material; under this assumption:

$$L_k = \frac{\mu_0 \lambda_L^2}{t} \quad (4)$$

Actually, since in our case  $\lambda_L = 16 \text{ nm}$  and  $t = 60 \text{ nm}$ , we are working between the limits of  $t \ll \lambda_L$  and  $t \gg \lambda_L$ , so we have:

$$L_{tot} = L_k + L_m = \frac{\mu_0 \lambda_L}{2} \coth \frac{t}{2\lambda_L} \quad (5)$$

For both cases we have a crucial dependence on  $\lambda_L$ , because the responsivity of KIDs is determined by the change in internal inductance of the superconductive film, corresponding to a change in Cooper pairs density and consequently in  $\lambda_L$ . As we could expect, the fractional surface impedance is comparable to the fraction of Cooper pairs that are broken:

$$\frac{\delta L_{tot}}{L_{tot}} \approx \frac{\delta n_{qp}}{2n_{cp}} \quad (6)$$

where  $n_{cp}$  is the density of Cooper pairs, and  $n_{qp}$  is the density of quasi-particles, which are the unpaired particles considered as superpositions states of electrons and holes.

### 3 Working principle

As we have already pointed out, KIDs can detect incoming particles thanks to the properties of a LC superconducting circuit (shown in figure 1). Now we are ready to describe their working principle in a deeper way.

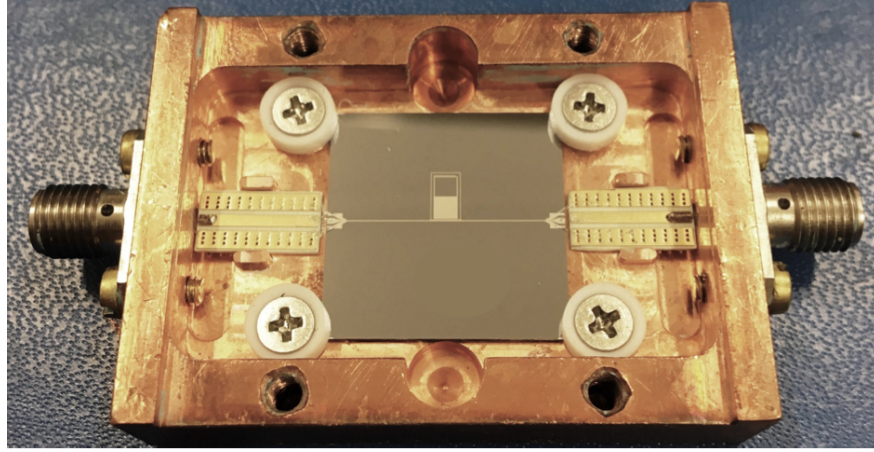


Figure 1: A single KID deposited on a  $2 \times 2 \text{ cm}^2$  Si substrate.

KIDs are biased with AC current, so Cooper pairs are oscillating: this oscillation guarantees a certain amount of kinetic inductance. When a particle or a phonon arrives in a KID, it is absorbed by the superconducting film, where it breaks Cooper pairs creating a number of quasi-particle excitations (see fig. 2.a). This build-up of quasi-particle density causes an increase of kinetic inductance. In order to quantitatively measure this effect, the superconductor is coupled with a capacitor, to realize a LC circuit (see fig. 2.b): this acts like a resonator with a resonance frequency:

$$f_0 = \frac{1}{2\pi\sqrt{LC}} \quad (7)$$

where  $L = L_{tot}$  and with a high quality factor Q of  $10^4$ - $10^5$ . Therefore a change in the internal inductance will modify the condition of the resonator leading to a new resonant frequency. The resulting fractional change in the resonance frequency  $f_0$  is expressed as:

$$\frac{|\delta f|}{f_0} = 0.5\alpha \frac{\delta L_{tot}}{L_{tot}} \quad (8)$$

where  $\alpha$  represents the fraction of the total inductance of the transmission line that is contributed by the kinetic inductance:

$$\alpha = \frac{L_k}{L_{tot}} \quad (9)$$

The effect of the incoming particle is actually twofold: the quasi-particles increase both the inductance and the resistance of the surface, which moves the resonance to a lower frequency (due to  $L$ ) and makes the dip broader and shallower (due to  $R$ ) (see fig. 2.c). Both of these effects also contribute to changing the phase and the amplitude of a microwave probe signal transmitted through the circuit (see fig. 2.d). As a result, it is possible to infer the energy that was deposited by monitoring the changes in the resonance parameters (the amplitude and the phase).

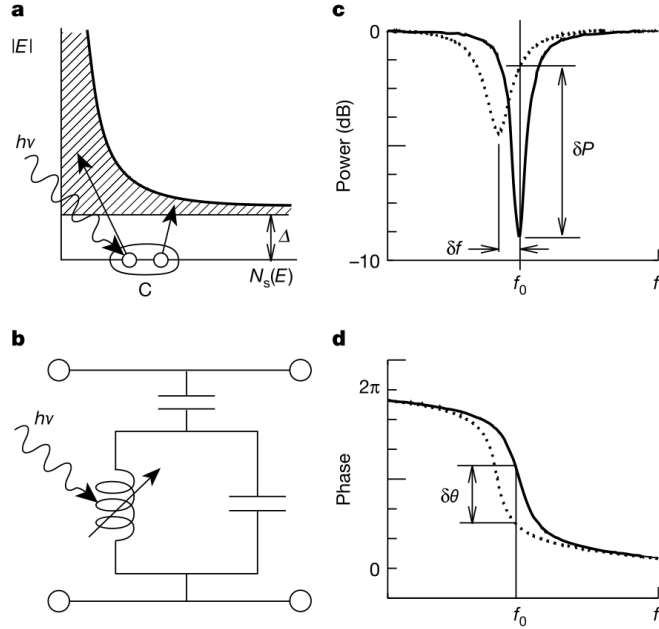


Figure 2: An illustration of the detection principle. Adapted from [2].

The main limitation of KIDs is the restricted active area, so an indirect detection system is added in order to overcome this issue: the single KID is deposited on a large insulating substrate (Si) that mediates the particle interactions converting them into athermal phonons. The phonons that are not thermalized or lost through the substrate supports reach the superconductor and break some Cooper pairs, giving rise to the signal. This procedure is known as phonon-mediated approach and it guarantees an active area of the order of several  $cm^2$  instead of few  $mm^2$ .

## 4 Experimental setup

Our task was to design and implement a readout for a single KID and to take and analyze some data. However, before describing our work, it is important to go into further detail in the explanation of the cryogenic apparatus which contains the KID.

### 4.1 Cryostat

As we have already pointed out, KIDs are based on superconducting materials, so we need cooling devices to reach around 10% of their superconducting transition temperature  $T_c$ . Since our KID architecture is based on an aluminium resonator, the required range can be reached using a dry  $^3\text{He}/^4\text{He}$  dilution refrigerator with a base temperature of  $10\text{ mK}$  and radiative shields at  $600\text{ mK}$  and  $4.2\text{ K}$  (see fig. 3).

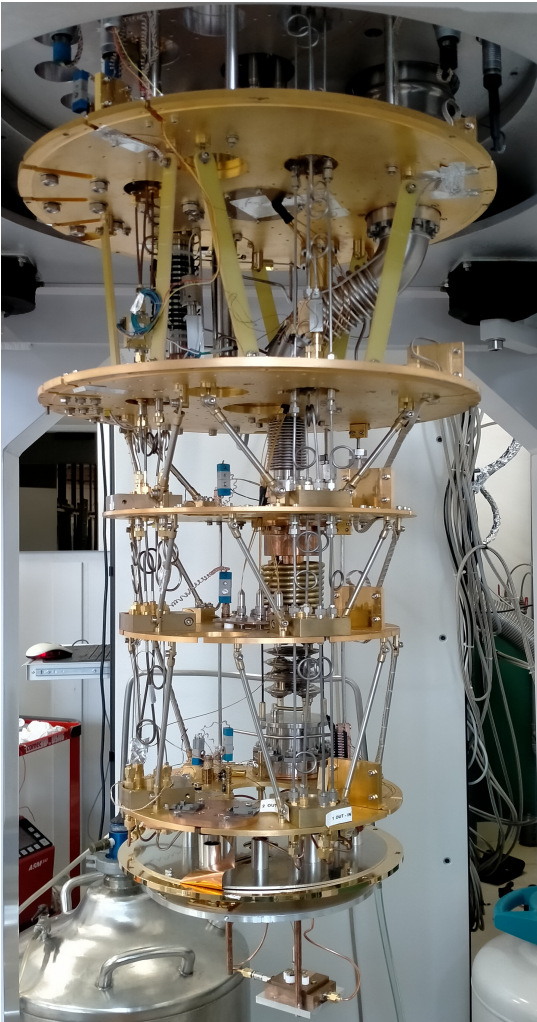


Figure 3: Cryostat setup.

ward. If the  $^3\text{He}$  is removed from the diluted phase,  $^3\text{He}$  atoms from the concentrated phase

In order to construct a refrigerator based on the dilution process, it is necessary to accomplish two primary aims: first, a mixture of  $^3\text{He}/^4\text{He}$  in the correct proportions must be allowed to condense and undergo a phase separation and secondly, the  $^3\text{He}$  must be preferentially recycled from the dilute  $^4\text{He}$ -rich phase, recondensed, and then returned to the concentrated  $^3\text{He}$ -rich phase. Concerning the correct proportions, the dilute phase contains about 6.6%  $^3\text{He}$  and 93.4%  $^4\text{He}$ . Regarding the  $^3\text{He}$  cycle instead, it starts when the isotope enters the cryostat at a pressure of a few hundred millibar (reached with the help of vacuum pumps at room temperature) and it is precooled and purified by liquid nitrogen at  $77\text{ K}$  and then cooled by a pulse tube (PT) at  $4\text{ K}$  and further cooled at about  $2 - 2.5\text{ K}$  by a Joule-Thomson expansion. This is enough to condensate both  $^3\text{He}$  and  $^4\text{He}$ . Next, the isotope flow exchanges heat with the still at a temperature between  $0.5$  and  $0.7\text{ K}$  and then it is further cooled down in a set of counter-flow heat exchangers by a cold flow of  $^3\text{He}$  moving in the opposite direction. Eventually, the pure  $^3\text{He}$  enters the mixing chamber where the  $^3\text{He}/^4\text{He}$  mixture is kept at a temperature that allows to maintain two separate phases: one  $^3\text{He}$ -rich phase floating on top and the other  $^4\text{He}$ -rich heavier phase downward.

will cross the phase boundary to occupy the vacant energy states. This process is called dilution and the heat it needs to happen is the cooling power of the refrigerator.

Concerning the cold electronics, the sensor, working at  $20\text{ mK}$ , is followed by a low noise cold amplifier (LNA) operated at  $4\text{ K}$ . Due to the low-temperature working conditions, the KID is at thermal contact with the coolest golden plate inside the cryostat. In addition, in order to protect the chip from external radiation and to realise a shield from inner thermal radiation, the plates are isolated by several nested screens (the external one is shown in fig. 4).



Figure 4: A view of the cryostat from outside.

## 4.2 Readout concept

Our readout was based on the so-called homodyne detection, which exploits the comparison of a Radio Frequency signal (RF), carrying some low frequency information on top of a particular RF sinusoidal signal (the so-called Local Oscillator or LO), with respect to the Local Oscillator itself.

In other words, the readout consists in extracting the baseband frequency signal from the RF signal, by simply subtracting in frequency the RF signal from the LO one, similarly to what happens with the frequency modulation radio.

This frequency subtraction is achieved using a non-linear circuit element such as the IQ mixer, which outputs the I (in-phase) and Q (quadrature) components of the signal, corresponding to its real and imaginary part. These two channels, at baseband frequency, are then easily sampled by an Arduino Due microcontroller. Then, the signal phase is reconstructed and the height of the phase pulses, proportional to the energy absorbed by the resonator, is eventually analyzed.

As shown in figure 5 and 6, our design of the readout consists in three sections: an RF and a baseband circuit (mounted on a prototype breadboard), followed by a two-channel digitizer, that is the ADC of an Arduino DUE. The microcontroller is capable of sampling at about 333 kHz, but it is limited to 206 kHz in the real data-taking in order to be able to also act as an online trigger.

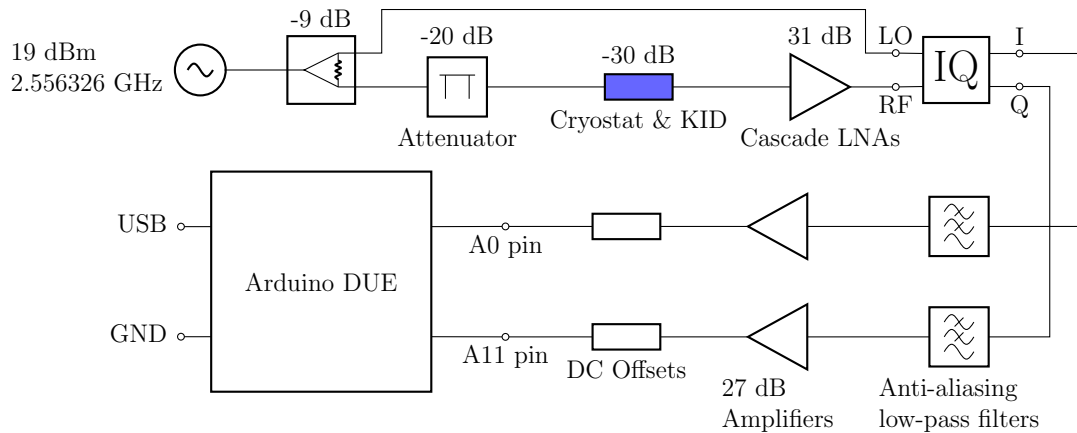


Figure 5: Homodyne Readout schematic. Note that the two channels are connected to the ADC using the two most distant pins (A0 and A11) in order to avoid crosstalks, that the laptop is connected to the Native USB port of Arduino and that the low-noise amplifiers (LNA), all the op-amps and Arduino share the same ground line.

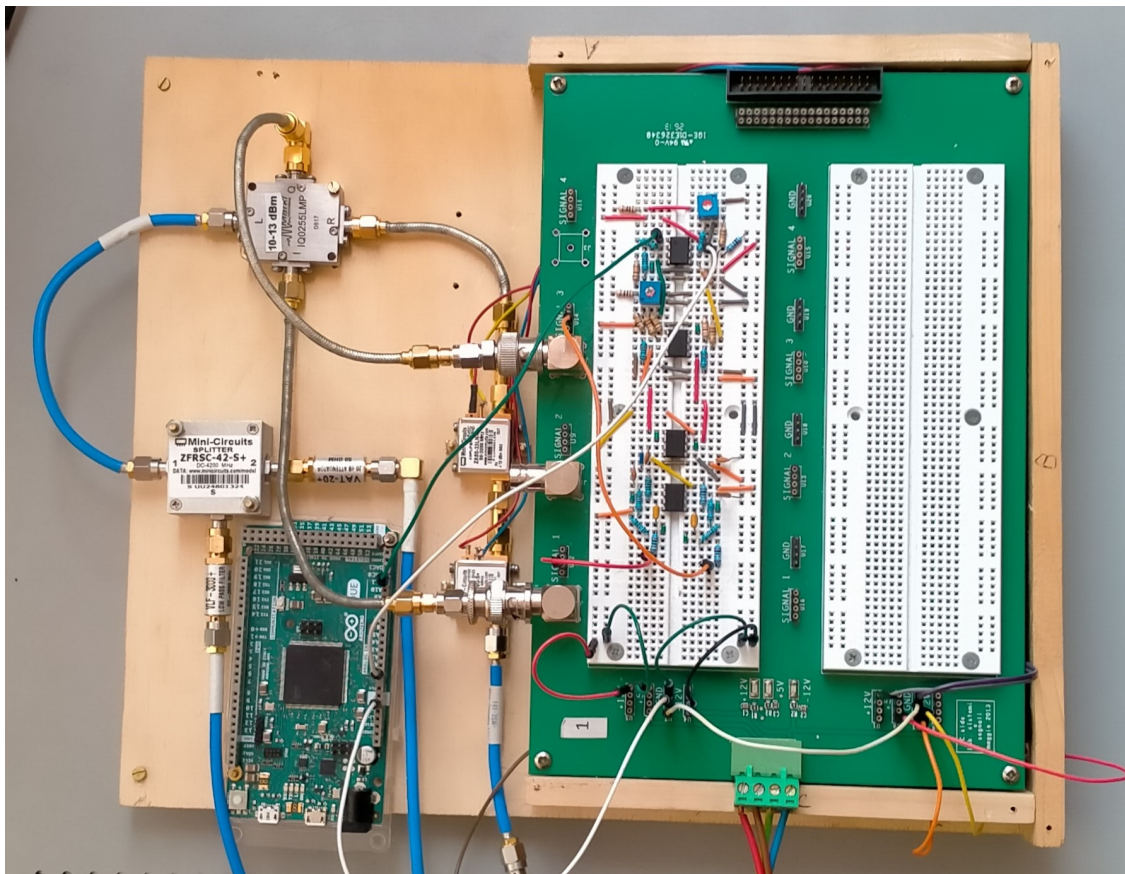


Figure 6: Complete readout system picture. Before the data-taking, several flexible jumpers were replaced with rigid ones (not shown in figure) to reduce the noise generated by vibrations.

## 4.3 Radio frequency circuit

A radio frequency synthesizer (Agilent MXG Analog Signal Generator N5182B) generates the LO cosine signal, which is divided by a power splitter into two copies with a 9dB loss. One of the two channels goes into the LO port of an IQ mixer, while the other one is attenuated by 20dB before entering the cryostat (in order to match the correct working point of the resonator), passes through the KID resonator and then goes through a 40dB CITLF3 SiGe cryogenic low noise amplifier. The whole cryostat provides an attenuation of about 30dB to the baseline, in addition to the stopband effect of the resonator. Outside the cryostat, at room temperature, the RF signal is amplified by 31 dB by a couple of cascade low-noise amplifiers, and then goes in the RF port of the IQ mixer, as shown in figure 5.

### 4.3.1 IQ mixer

The IQ mixer is a Marki Microwave IQ0255LMP and consists of two identical down-conversion mixers where the RF ports are connected with an in-phase power splitter and the LO ports are connected with a quadrature hybrid, a special power splitter that also creates a  $90^\circ$  phase shift between the two outputs, as shown in figure 7.

As it will be explained, for an ideal IQ mixer the outputs are the real part, in the I (in-phase) channel, and the imaginary part, in the Q (quadrature) channel, of the baseband frequency signal.

The output of a normal mixer, unlike an IQ one, is the product of the two inputs. By exploiting the trigonometric Werner formulas we know that:

$$A(t) = \sin \omega_1 t, B = \sin \omega_2 t \Rightarrow A(t)B(t) = \frac{1}{2} [\cos(\omega_1 + \omega_2)t - \cos(\omega_1 - \omega_2)t] \quad (10)$$

In the down-conversion mixer, we only obtain a signal at a frequency given by the difference of the LO and RF frequencies, because the  $\cos(\omega_1 + \omega_2)t$  component is suppressed.

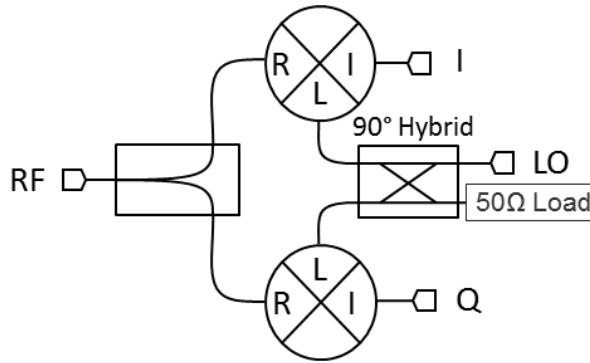


Figure 7: IQ mixer schematic.

More specifically, if:

$$LO(t) = a_{LO} \sin(\omega_{LO}t), RF(t) = a_{RF} \sin(\omega_{RF}t + \phi) \quad (11)$$

where the  $a_{RF}$  and  $\phi$  also depend on time but at a much lower frequency (e.g. kHz) with respect to  $\omega_{LO}$  (e.g. GHz), then:

$$LO(t) \cdot RF(t) = a_{LO}a_{RF} \sin(\omega_{LO}t) \sin(\omega_{RF}t + \phi) \quad (12)$$

$$= \frac{a_{LO}a_{RF}}{2} \left( \cos((\omega_{RF} - \omega_{LO})t + \phi) - \cos((\omega_{RF} + \omega_{LO})t + \phi) \right) \quad (13)$$

and:

$$LO(t + \frac{\pi}{2}) \cdot RF = a_{LO}a_{RF} \cos(\omega_{LO}t) \sin(\omega_{RF}t + \phi) \quad (14)$$

$$= \frac{a_{LO}a_{RF}}{2} \left( \sin((\omega_{RF} - \omega_{LO})t + \phi) + \sin((\omega_{RF} + \omega_{LO})t + \phi) \right) \quad (15)$$

For  $\omega_{LO} = \omega_{RF}$  and suppressing the  $2\omega_{LO}$  components, we can define:

$$I = \frac{a_{LO}a_{RF}}{2\Lambda_I} \cos(\phi) \quad (16)$$

$$Q = \frac{a_{LO}a_{RF}}{2\Lambda_Q} \sin(\phi) \quad (17)$$

where the two  $\Lambda$ s are dimensional constants.

Note that both  $a_{RF}$  and  $\phi$  (amplitude and phase of the RF signal) are functions of frequency because of non-linear effects and the finite speed of the signal ( $\sim 0.7c$ ), which implies that the same transmission line phase-shifts the signal differently at different frequencies. Moreover, the IQ mixer is a real object, therefore the ideal behaviour is valid only in a range of frequencies (2.0 - 5.5 GHz in our case).

For these reasons, an initial calibration is needed to evaluate the offsets, the amplitudes and the conversion losses for the two channels of the mixer. These parameters will be needed in the choice of the elements in the baseband frequency circuit, which is essential in order to exploit the complete dynamical range (0-3.3V) of the ADC.

The calibration was made by introducing different phase-shifts in the RF signal using a 4m long coaxial cable as transmission line, while operating a frequency sweep in the range 2.180-2.217 GHz through the RF generator, at an amplitude of 19 dBm. A Keysight FieldFox RF Vector Network Analyzer (VNA) was used for diagnostics during the circuit construction. We also attenuated the signal by 30 dB to simulate the presence of the cryostat, as shown in figure 8. The RF amplitude, measured at the mixer input with the VNA, is equal to -8.791(3) dBm, corresponding to about 115 mV.

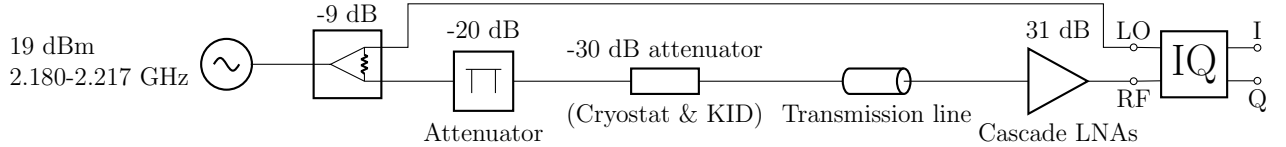


Figure 8: RF circuit schematic for the IQ mixer calibration.

The I and Q channels were read using a Keysight DSOX1204G oscilloscope and visualized in the I-Q plane, as shown in figure 9.

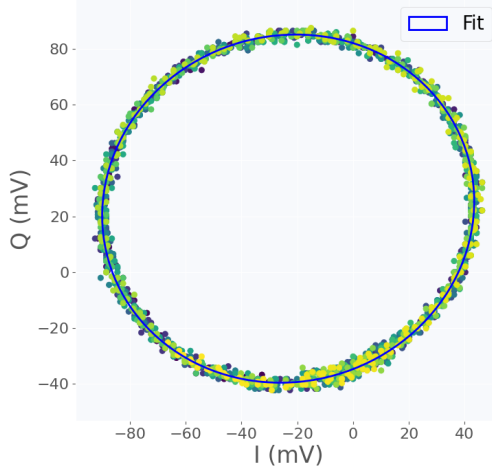


Figure 9: I and Q scatter plot for the loopback measurement and ellipse fit, using the formula  $\left(\frac{I-I_c}{I_a}\right)^2 + \left(\frac{Q-Q_c}{Q_a}\right)^2 = 1$ .

Theoretically the resulting curve should be a circle, but the mixer has different conversion losses for I and Q, so the data was fitted with a slightly eccentric ellipse, with parameters  $I_c = -23.255(3)$  mV,  $Q_c = 22.267(3)$  mV,  $I_a = 67.009(2)$  mV and  $Q_a = 61.908(2)$  mV.

#### 4.4 Baseband circuit

Since the goal was to sample with an Arduino Due, which has a dynamical range of 0-3.3 V, it was necessary to design a baseband circuit in order to both maximize the dynamics of the signal and to make sure that all the sampled points fell in the 0-3.3V square in the IQ plane. The circuit was implemented in two copies, one for each channel, and mounted on a single prototype breadboard, as shown in figure 10.

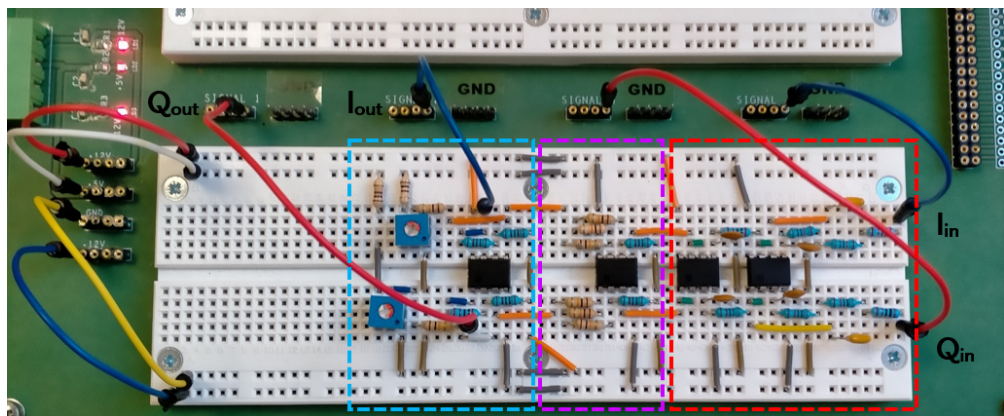


Figure 10: Complete baseband circuit view: the I channel is processed in the upper half of the breadboard and the Q channel in the lower one. The colored boxes are: **anti-aliasing filters**, **amplifiers** and **summing circuits**.

#### 4.4.1 Anti-aliasing filter

First of all, the signal passes through a third-order anti-alias Bessel filter, shown in figure 11. Considering that the pulses generated during the absorption of energy have characteristic frequencies up to 40 kHz and knowing that Arduino's sampling rate is around 330 kHz, the passband (-3dB) and stopband (-20dB) frequencies were respectively set to 50 kHz and 160 kHz. In the real data-taking, when the ADC works at 206 kHz, the filter response is -17 dB at the Nyquist frequency, so we consider it still sufficient to suppress the aliases.

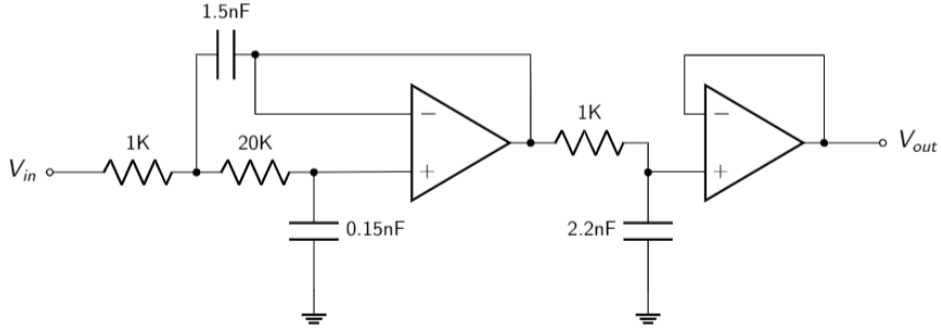
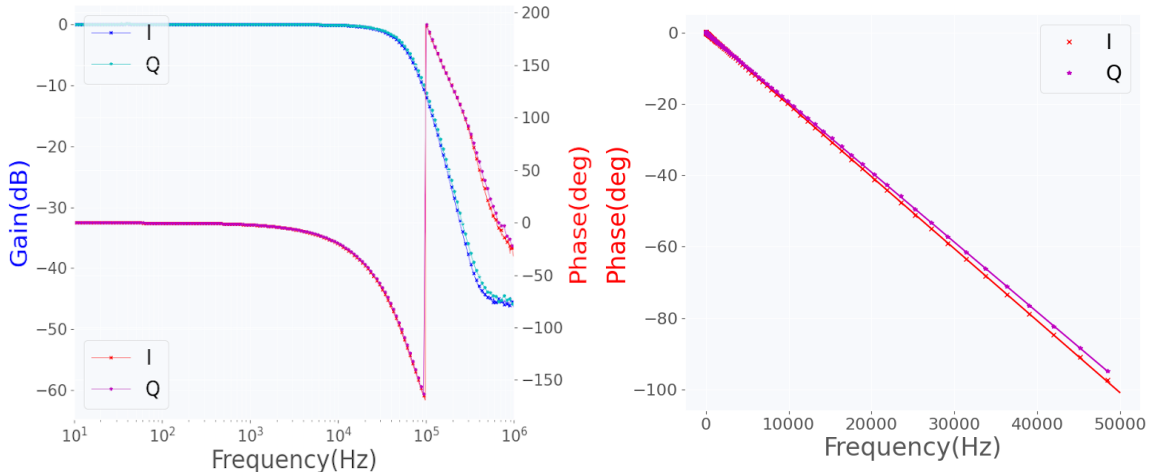


Figure 11: Bessel circuit schematic. The filter is composed by two stages: a second-order Sallen-Key and a first-order buffered RC. The op-amp used is a TL-082.

After building the filters, the requirements were verified with the oscilloscope using the frequency response function. The flatness of the group delay, i.e. the linearity of the phase response, has been checked through a linear fit in the signal band. As shown in figure 12, the type of filter designed permitted to achieve a roll-off of 60 dB/Decade (estimated knowing that the response is -11dB at 100kHz and -40dB at 300 kHz), as expected for a third-order filter, and a maximally flat group delay (as expected for a Bessel filter).



(a) Gain and phase (modulo  $\pm 180^\circ$ ) responses. (b) Phase responses linear fits up to 50 kHz.

Figure 12: Anti-aliasing filters characterization.

#### 4.4.2 Amplifier and Summing Circuit

We also developed a simple non-inverting amplifier with a gain of 27dB followed by a summing circuit (shown in figure 13), to maximize the signal range, starting from  $Q_{pp} < I_{pp} < 140$  mV (see 4.3.1), while keeping the values contained in the ADC range of 0-3.3V.

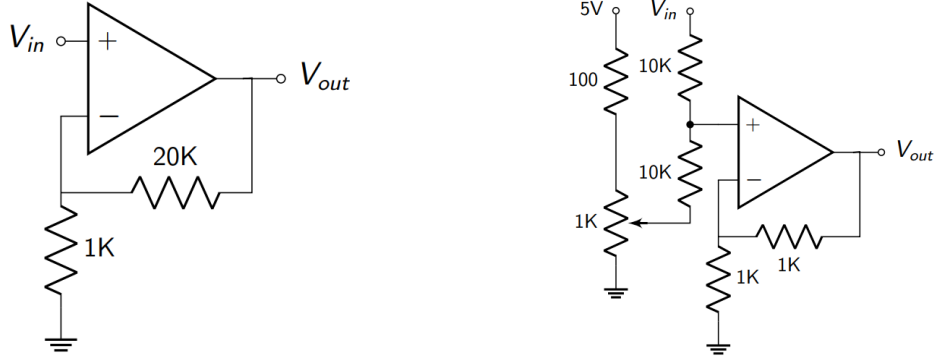


Figure 13: Non-inverting amplifier (on the left) and summing circuit (on the right) schematics.

The complete circuit response has been measured through the oscilloscope, as shown in figure 14, and the requirements have been successfully verified.

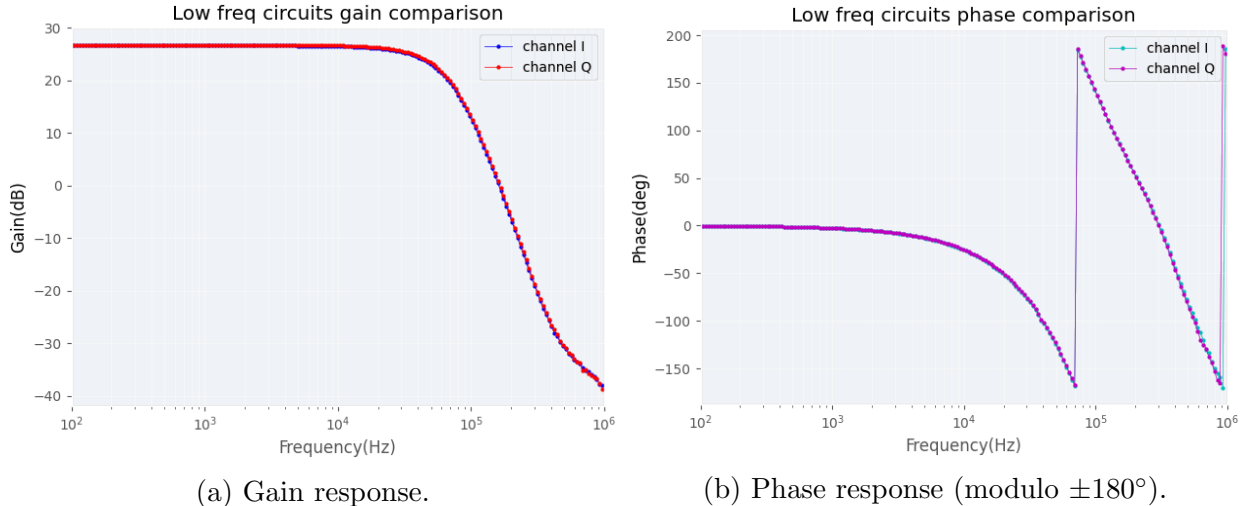


Figure 14: Complete circuit responses.

### 4.5 Data Acquisition

#### 4.5.1 Digitizer

Our DAQ hardware consists in an Arduino DUE connected to a laptop running a Python script. The microcontroller samples two analog channels via its internal 12 bit ADC. We set the ADC registers to the Free-Run mode, in which the conversions are continuously performed

(at the maximum speed allowed by the ADC clock) and an interrupt signal is called as soon as the digital value is available. This setting lets the sampling rate increase from 100 kHz (using the usual analogRead function) to 333 kHz.

#### 4.5.2 Online trigger

In order to reduce the amount of data to transmit out of Arduino, an online trigger is needed. Our triggering algorithm consists in smoothing the waveforms through a moving average over a window of 10 samples and triggering with a threshold on the derivatives of I (calculated as  $(I_n - I_{n-10})/10$ ). As a matter of fact, since Arduino's handling of floating point is quite slow, we preferred to apply the cut just as  $(I_n - I_{n-10}) > \text{threshold}$  after the smoothing. Note that the transmitted data are not smoothed, because we need the raw values to perform a finer analysis offline.

The threshold is calculated (at the beginning of the data taking) as 5.8 times the standard deviation of the derivative of the smoothed noise. The value of 10 has been chosen because it is the number of points contained in the signal rise. On the other hand, the value of 5.8 has been chosen (through a simulation of the trigger on non-triggered data) to have a very low false negative rate (nearly all the real signals are saved) and a low false positive rate (30% of the saved signals only contain noise). For these reasons, a more involved offline selection is applied afterwards.

Unfortunately, Arduino DUE's clock is rather slow (84 MHz), so the smoothing procedure slows down the data taking to 206 kHz, as shown in figure 15 and 16.

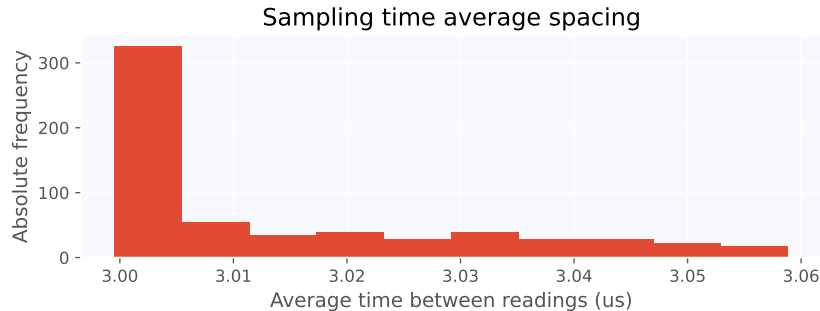


Figure 15: Sampling time average spacing ( $\Delta T/N$ ) without smoothing for  $\sim 600$  signals. It corresponds to a sampling rate of nearly 333 kHz.

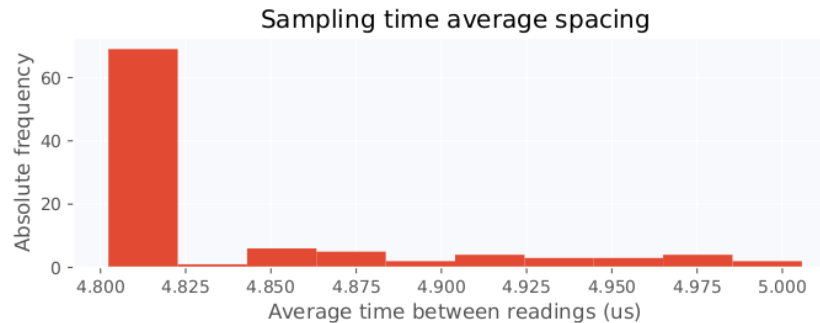


Figure 16:  $\Delta T/N$  in the real data-taking for  $\sim 100$  signals. The average time difference is  $(4.842 \pm 0.052)\mu\text{s}$ , which corresponds to a rate of  $(206.5 \pm 2.2)$  kHz.

### 4.5.3 DAQ procedure

Every acquired sample is put in a circular buffer of 3333 elements, which corresponds to a recording time of 16 ms. After the trigger, 2667 samples are acquired, until the whole buffer (which also contains 666 samples acquired before the trigger) is sent, as bytes, to the USB port connected to the PC. The buffer was dimensioned (before the implementation of the trigger) to record 10 ms of data at the original sampling rate of 333 kHz.

The time needed to transmit the data over the USB is the dead time of our DAQ procedure, and it is of the order of 5 ms, as shown in figure 17.



Figure 17: Acquisition dead time histograms in a typical use case: the first one (in log-log scale) shows all the distribution, that contains many outliers due to operative system disturbances, while the second only shows its major part.

The Python script, running on a laptop, decodes the data and saves the content of the buffer in a text file, containing the values of I and Q and the timestamp of each sample (in microseconds from the beginning of the data taking).

It is important that the script and the Arduino program are somehow synced. This is achieved through an handshake procedure (as shown in figure 18), in which the script sends to Arduino the acquisition time duration, and receives back the trigger threshold. This way, not only these two useful pieces of information are shared, but also Arduino starts sending bytes only when the script is ready to receive them, in order to avoid dangerous misalignments.

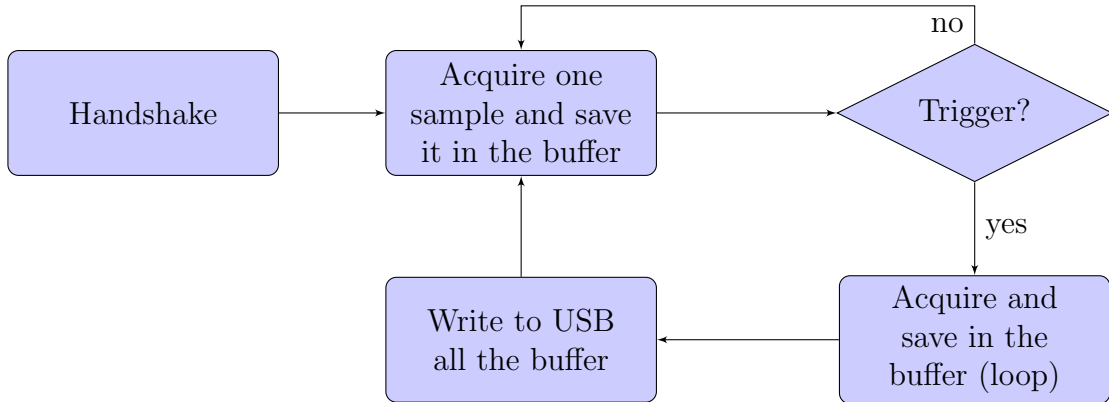


Figure 18: DAQ flow chart.

Another important point is that the laptop must be disconnected from the power supply, so as to avoid the noise from the 220V line (caused by unresolved grounding issues), which affects the Arduino ADC reference voltage and makes the recorded data useless, as we have experienced during the first tries.

## 5 Data Analysis

### 5.1 IQ mixer calibration

To calibrate the IQ mixer in the real experimental situation, we connected the apparatus to the KID and operated a frequency sweep in the range 2.555-2.558 GHz, which contains the resonance frequency of our KID (2.556326 GHz). The resulting ellipse in the I-Q plane was fitted (see fig. 19), getting the parameters:

- I and Q offset:  $I_c = 1.5742(1)V$  and  $Q_c = 0.6235(1)V$
- I and Q axis:  $I_a = 0.4110(2)V$  and  $Q_a = 0.4306(2)V$

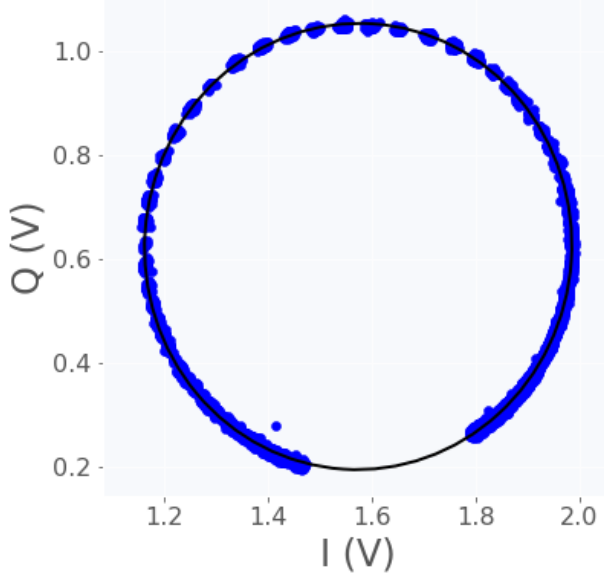


Figure 19: Ellipse fit in the I-Q plane.

After subtracting the I and Q offset, the I-Q unbalance of the IQ mixer is corrected scaling the Q values by the ratio of the I and Q axis, by means of the formulas:

$$Q \rightarrow \frac{I_a}{Q_a}(Q - Q_c) \quad (18)$$

$$I \rightarrow I - I_c \quad (19)$$

This converts our ellipse into a circle, therefore the phase can be evaluated simply as:

$$\phi = \arctan\left(\frac{Q}{I}\right) \quad (20)$$

## 5.2 Signals reconstruction

The detector response in energy is proportional (in a certain range) to its response in phase and amplitude. We chose to analyze the events using only the heights of the phases pulses with respect to the baseline, estimated as the average over the first 500 points of each acquisition, which most probably do not contain pulses because the post-trigger samples are located after the 667th sample of each acquisition.

### 5.2.1 Signal sources

We analyzed the detector response to three types of energy deposition:

- Unavoidable cosmic rays passing through the absorber and natural radioactivity, not analyzed in detail.
- X-rays coming from a very low-activity Fe-55 source on the absorber (shown in figure 20). This isotope decays via electron capture to Mn-55 with a half-life of 2.737 years. It emits Auger electrons of 5.19 keV, with a probability of about 60%, K-alpha-1 X-rays of 5.89875 keV with a probability about 16.2%, K-alpha-2 X-rays of 5.88765 keV with a probability of about 8.2%, or K-beta X-rays of 6.49045 keV with a probability of about 2.85%.

The energies of the K-alpha-1 and -2 X-rays are so similar that they are often specified as mono-energetic radiation with 5.9 keV photon energy and probability of about 28%. Unfortunately our apparatus is not capable of distinguishing the peaks, because all of them are very spread (more than our detection resolution), due to the geometry of the source and detector. Moreover, the Auger electrons are not detectable because a plastic film (scotch tape) covers our source.

- 400nm light pulses, sent to the resonator in 50ms-spaced bunches via an optical fiber. The light source is controlled through a signal generator in burst mode, so that the number of photons  $n$  in each bunch, which represents the light intensity, is proportional to the easily adjustable number of pulses in the bursts, also called cycles.

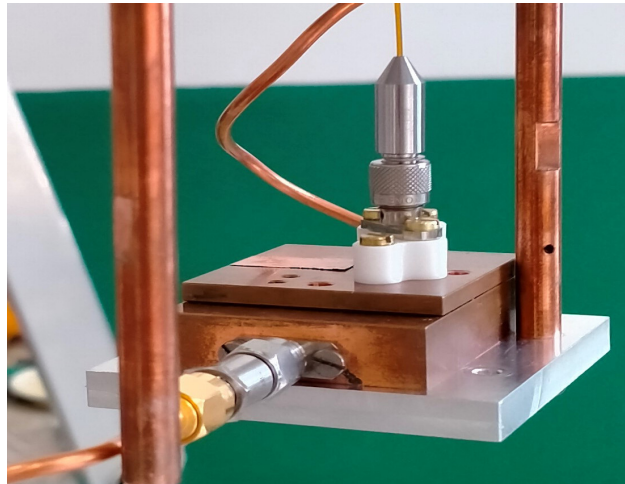


Figure 20: KID apparatus, with the optical fiber and the radioactive source on top.

### 5.2.2 Smoothing

In order to carefully evaluate the phase pulses height, we firstly need to smooth the signals and to select the events in a better way. For these reasons, we evaluated the noise spectral density of the phase signals, reported in figure 21:

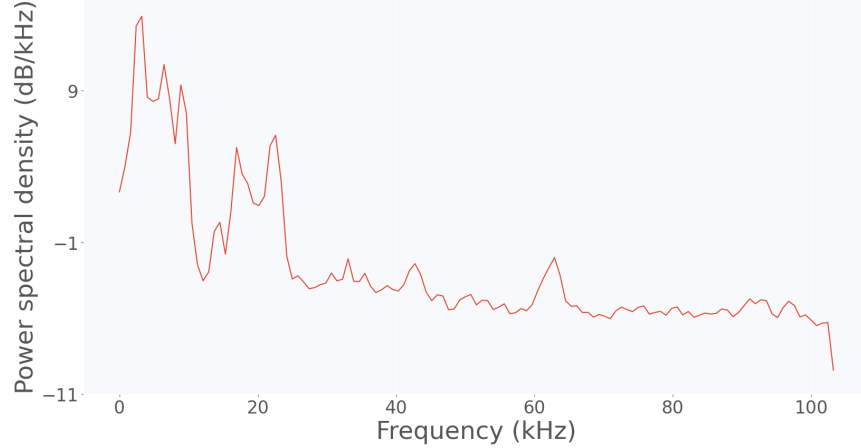


Figure 21: Phase noise spectral density, estimated using the Welch's method. Note that the noise has been retrieved by the pre-pulse window of 666 samples in each file.

The two noisiest regions are located near 2.5 kHz and 20 kHz, therefore they contain some of the characteristic frequencies of the signals. Then, we just needed to smooth the signals, in order to keep the pulses visible and to suppress the noise. For the sake of simplicity we chose to use a moving average with a window of 70 points, as shown in figure 22.

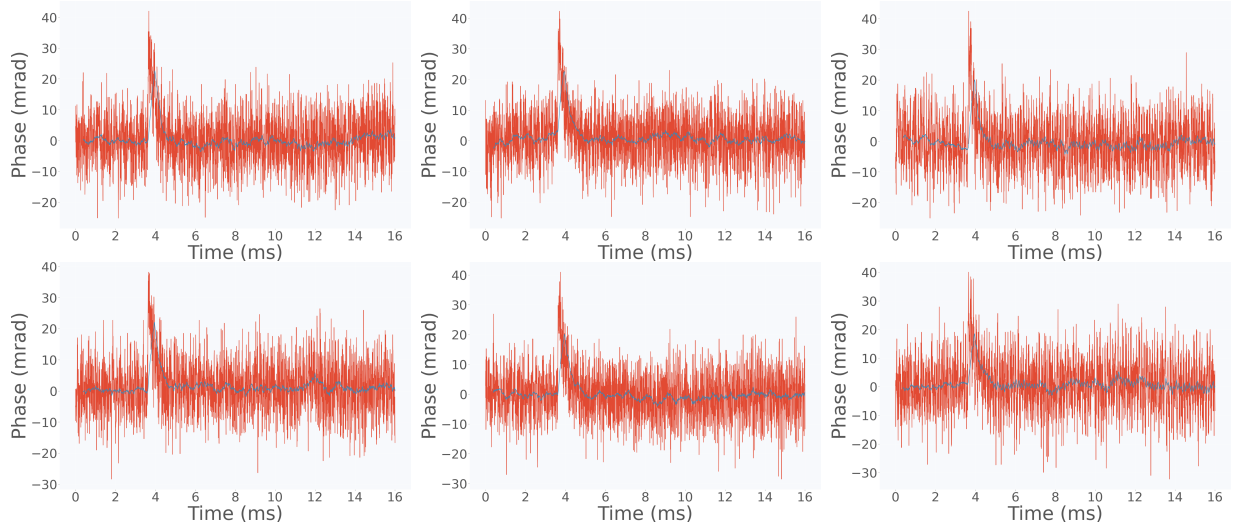


Figure 22: Some of the pulses selected, showing in red the non-smoothed phase waveform and in blue the smoothed one.

The value of 70 for the window has been chosen because it provided a good uncertainty on the phase response to light pulses, as shown in figure 23.

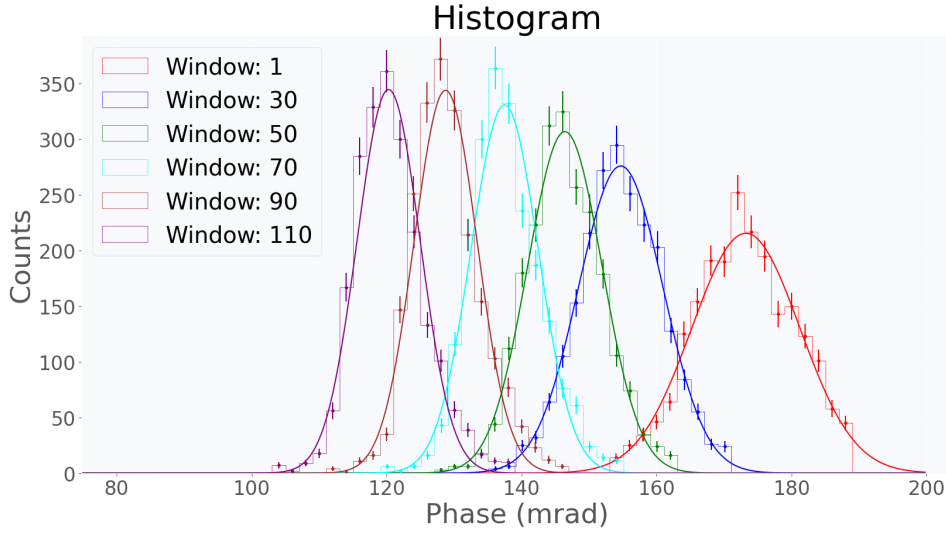


Figure 23: Histograms of phase response to light pulses (2 cycles) for several different windows, fitted with gaussians. The uncertainties with a window of 70, 90 or 110 are extremely similar, so we decided to use a window of 70 in order to have a faster time response.

As the pulses height is lowered by this smoothing procedure, we must multiply them by a gain factor, which is the average ratio between the height of the non-smoothed peak and the smoothed one. This factor is equal to  $1.296 \pm 0.002$  for a window of 70.

### 5.2.3 Events selection

The Arduino online trigger is not sufficient for our purposes, as it only provides a rough but very permissive trigger able to reduce the amount of data to handle.

However, our real event selection is based on the same method, working with the phases instead of the I values.

The window of the rolling average and the step of the derivative, which are equal to 10 in the online trigger, are kept both equal to 70, so we only have one parameter to optimize: the threshold.

First of all we recorded data for about 30 minutes without sending light pulses and, secondly, we visually selected the real events (the ones with a visible pulse in the waveform) out of the first 1000 files (16 ms acquisitions) obtained.

Then we leveraged this visual selection to optimize the threshold using the precision-recall curve method. It consists of finding the thresholds that maximizes both the precision and the recall, defined as:

$$\text{Precision} = \frac{tp}{tp + fp}, \quad \text{Recall} = \frac{tp}{tp + fn} \quad (21)$$

where  $tp$ ,  $fp$  and  $fn$  are, respectively, the true positive rate, the false positive rate and the false negative rate. In other words, in the recall-precision plane, we chose the threshold that minimizes the distance to the  $(1, 1)$  point. As shown in figure 24, the best threshold is 14 mrad and it provides a precision of 99.7% and a recall of 98%.

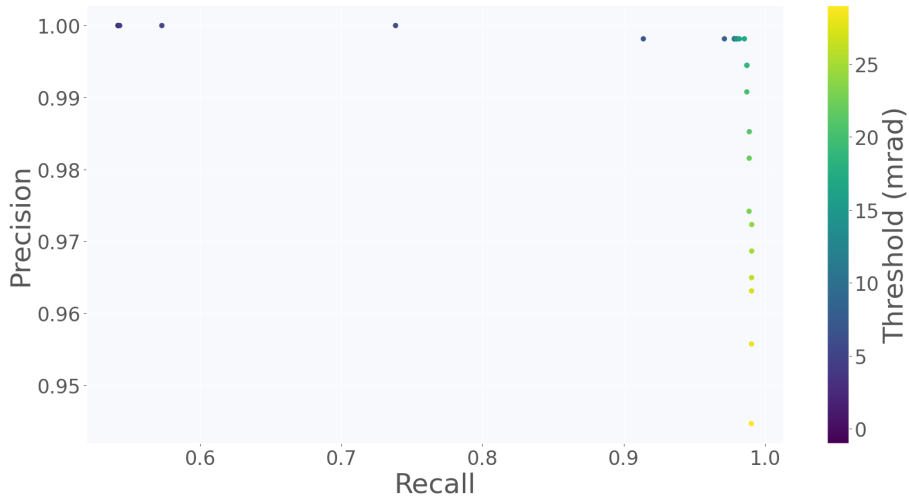


Figure 24: Precision-recall curve for 2000 acquisitions, with thresholds from 0 to 30.

### 5.3 Calibration

The phase response  $\phi = \frac{d\phi}{dE}E$  is proportional to the incident energy  $E$  in the detector, which is given by  $\epsilon n$ , being  $\epsilon = 3.1\text{eV}$  the photon energy at 400nm.

As  $n$  (which is a huge number) is Poisson-distributed,  $\delta E = \epsilon\sqrt{n}$ , in the absence of other sources of error; then  $\delta\phi = \frac{d\phi}{dE}\epsilon\sqrt{n}$ . Writing  $\phi$  as  $\phi = \frac{d\phi}{dE}\epsilon n$ , we can show that  $\sigma^2[\phi] = \frac{d\phi}{dE}\epsilon\phi$ . Including the effect of the finite resolution  $R_\phi$  of the detector, we obtain:

$$\sigma^2[\phi] = R_\phi^2 + \frac{d\phi}{dE}\epsilon\phi \quad (22)$$

Thus, to calibrate our detector, we only need to send to the KID light pulses with different numbers of cycles, evaluate the expected value and the variance of the phase peaks for each one, and fit  $R_\phi$  and  $\frac{d\phi}{dE}$  through the above formula. The number of cycles sent was in the range 1 – 6; unfortunately, due to DAQ problems, we had to discard the data-takings with 4 and 5 cycles. The mean and variance of the peaks has been estimated by fitting the histograms with gaussians, as shown in figure 25.

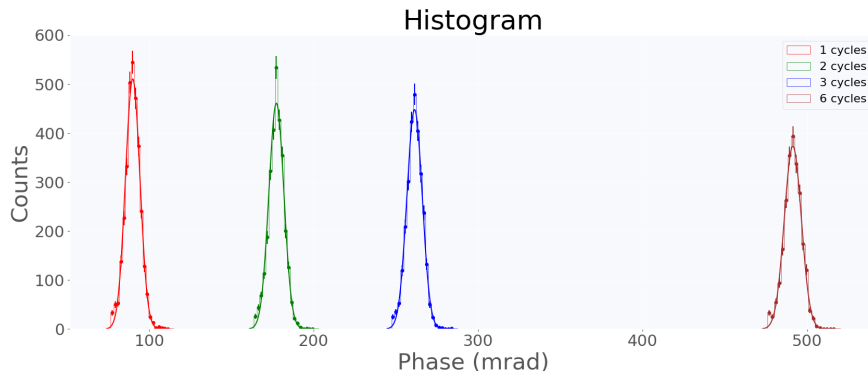


Figure 25: Histograms of the phase response to the light pulses, with gaussian fit.

Before making the calibration linear fit (in figure 27), we verified the linearity of the response, as shown in figure 26.

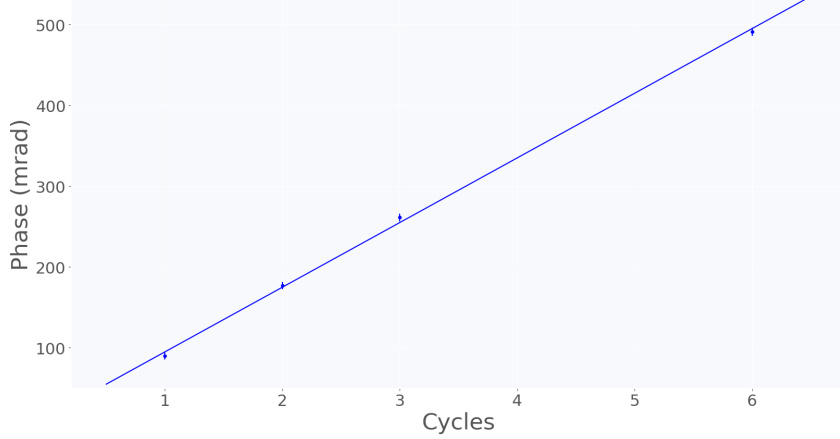


Figure 26: Peaks mean vs. number of cycles, to verify the linearity of the response.

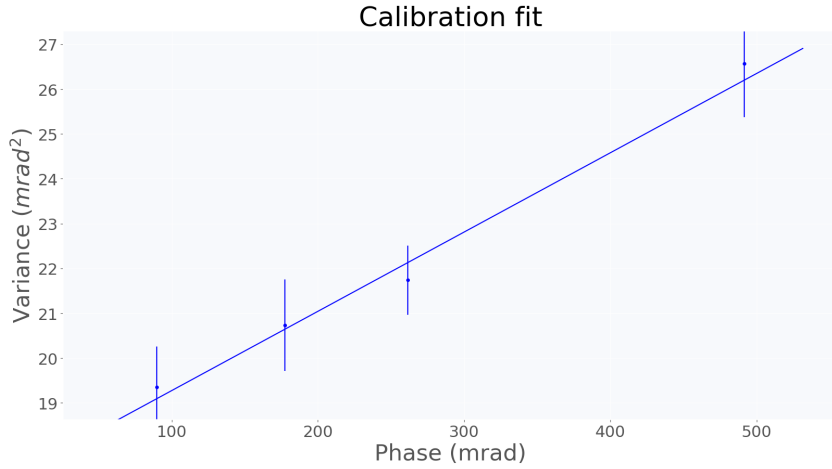


Figure 27: Calibration fit of  $\sigma^2[\phi]$  vs.  $\phi$ .

We obtained a  $\frac{d\phi}{dE}$  of  $(5.70 \pm 0.55)$  mrad/keV and a resolution in phase of  $R_\phi = (4.183 \pm 0.054)$  mrad, corresponding to a resolution in energy of  $(733 \pm 68)$  eV, which is very large compared to the result obtained in [3] (82 eV) using high-quality electronics.

## 5.4 Fe-55 X-ray peak search

In a 30-minutes-long data-taking we selected 1179 events, corresponding to a rate of 0.655 Hz. The histogram of the energy of these events reveals a peak at  $(6.0 \pm 1.9)$  keV. The fact that this peak does not contain noise is verified by plotting another histogram of the same data-taking, where the events are selected with a more permissive threshold of 7 mrad (instead of

14 mrad). The pedestal, as shown in figure 28, is only present with the lower threshold, is centered at about 0.8 keV and does not overlap with the peak. The hypothesis that this peak corresponds to the K-alpha X-ray of Fe-55 (with a small unresolved component of K-beta X-rays) is consistent because its energy should be 5.9 keV, which is perfectly compatible with the value fitted. The large uncertainty on the energy is due to the fact that every X-ray (uniformly distributed on the solid angle) enters the absorber with a different angle, therefore the distributions of athermal phonons on the KID (which is not in a symmetric position with respect to the source) is different for each X-ray.

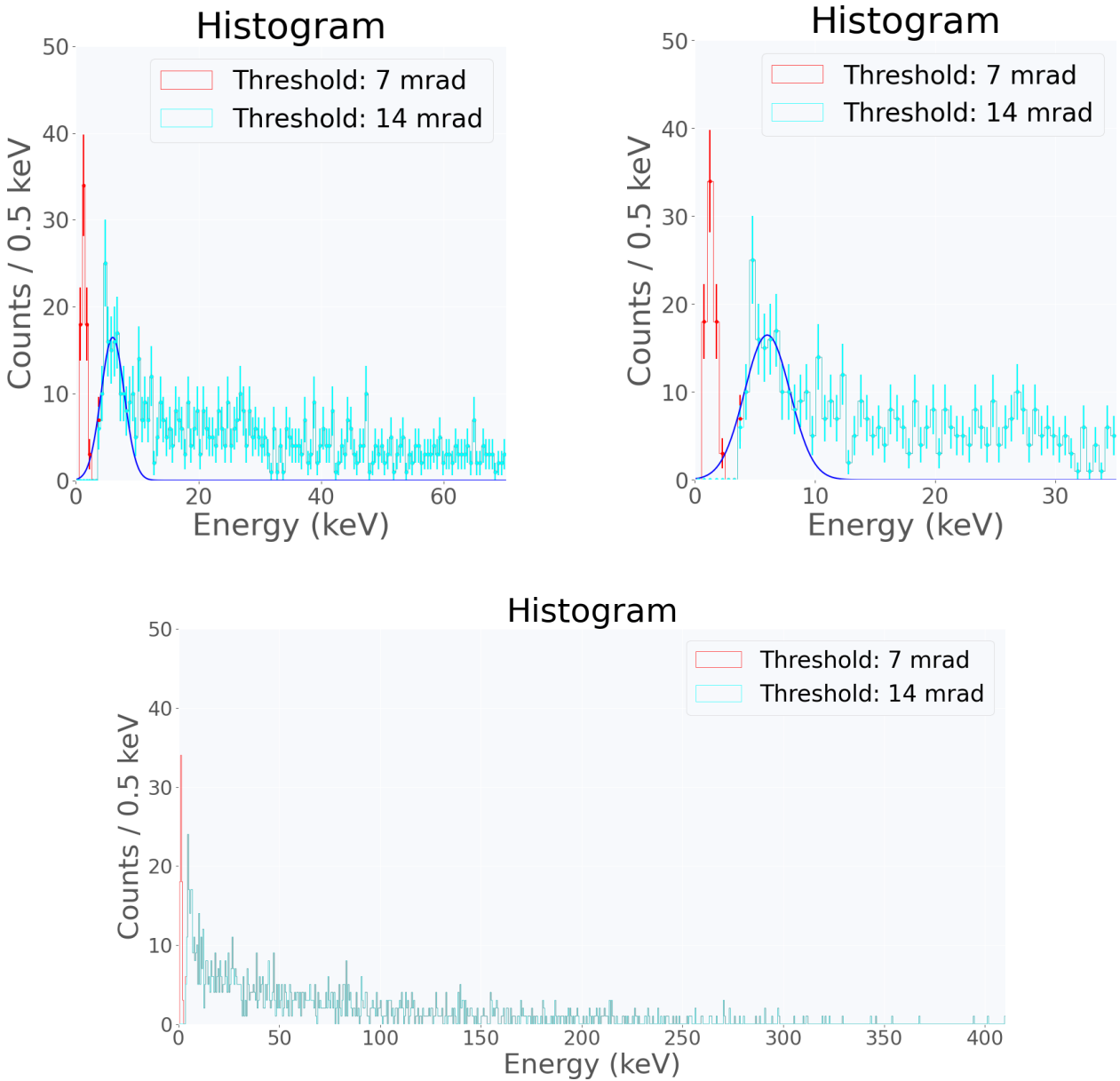


Figure 28: Histograms of the selected events for different ranges of values. The last histogram was not plotted with uncertainties (given by the Poissonian distribution) for the sake of visual clarity. Note that after the pedestal the red and blue histograms overlap completely.

## 6 Methods

All the fits without errors on the independent variable were made with the Least Squares method. In the cases in which also the independent variable is uncertain, we used the Orthogonal Least Squares method. The goodness of fits was verified through the Kolmogorov-Smirnov test for the normality of residuals, which outputs a p-value: the fit is rejected if  $p$  is less than 0.05 and is considered suspicious (because of a likely overestimation of the uncertainties) if  $p$  is greater than 0.95.

Some of the codes and the data used for the DAQ and the analysis are available on GitHub at the link: <https://github.com/raeubaen/kid>. Note that after several attempts, we discovered that the data-taking is cleaner when it is run on a Linux-based operative system, because it allows a more accurate control of the serial communications.

## 7 Conclusion

We started from the ground up and built our own readout system: it gave us the opportunity to really understand how the homodyne detection works and how to handle the various issues related to the DAQ.

We are really pleased with the results of the event selection algorithm, which let us observe the K-alpha X-ray peak of Fe-55 (5.89 keV) at  $(6.0 \pm 1.9)$  keV, and of the calibration, which gave good results: the  $\frac{d\phi}{dE}$  value we obtained  $((5.70 \pm 0.55)$  mrad/keV) is coherent with the result for the same KID from [3] (5.8 mrad/keV), although it is not very precise.

Nonetheless, we do not feel completely satisfied with our system: the main defects are lack of stability, difficulty of usage and large electronic noise. For these reasons using a printed circuit board instead of the solderless breadboard could have been a better solution.

One particular aspect that should be improved is the low resolution in energy ( $(733 \pm 68)$  eV), which is very distant from the result obtained in [3] (82 eV) using high-quality electronics for the readout.

## References

- [1] Day, P. et al. (2003). *A broadband superconducting detector suitable for use in large arrays.* Nature. 425 (6960): 817–821, .
- [2] Mazin, Benjamin A. (2005) *Microwave Kinetic Inductance Detectors*. Dissertation (Ph.D.), California Institute of Technology
- [3] L. Cardani et al. (2017). *High sensitivity phonon-mediated kinetic inductance detector with combined amplitude and phase read-out*. Appl. Phys. Lett. **110** (2017) no.3.
- [4] Calvo, M., Giordano, C., Battiston, R. et al. *Development of Kinetic Inductance Detectors for Cosmic Microwave Background experiments*. Exp Astron 28, 185–194 (2010).
- [5] Maloney et al. (2010). *MUSIC for sub/Millimeter astrophysics*. Millimeter, Submillimeter, and Far-Infrared Detectors and Instrumentation for Astronomy V. 7741. pp. 77410F.
- [6] Moore et al. (2012). *Position and energy-resolved particle detection using phonon-mediated microwave kinetic inductance detectors*. Applied Physics Letters, 100, 232601.
- [7] Colantoni et al. (2020). *BULLKID: BULky and Low-Threshold Kinetic Inductance Detectors*. Journal of low-temperature Physics, 199, 593.